Methylammonium Tetrafluoroborate Additive for Spontaneous Heterointerface Modulation in a Narrow-Bandgap $FAPbI_3$ Photoabsorber for Perovskite Solar Cells

Daisuke Kubota[†, §], *Ryuzi Katoh*[//], *Hiroyuki Kanda*[†], *Hiroyuki Yaguchi*[§], *Takurou N. Murakami*[†], *Naoyuki Nishimura*[†] *

† National Institute of Advanced Industrial Science and Technology (AIST),1-1-1 Higashi, Tsukuba, Ibaraki 305-8565, Japan.

§ Graduate School of Science and Engineering, Saitama University, Saitama-shi, Saitama 338-8570, Japan

// College of Engineering, Nihon University, Koriyama, Fukushima 963-8642, Japan

*Corresponding Author

Naoyuki Nishimura, E-mail: naoyuki-nishimura@aist.go.jp

ABSTRACT

Over the past decade, the photovoltaic (PV) performance of perovskite solar cells (PSCs) has been considerably improved with the development of perovskite photoabsorbers. Among these, formamidinium-lead-iodide ($FAPbI_3$) is a promising photoabsorber owing to its narrow bandgap and is mainly used in n–i–p-structured PSCs. The property modulation of $FAPbI_3$ photoabsorbers while retaining their narrow bandgap is imperative for further development of PSCs. Molecular tetrafluoroborate anion (BF_4^-)-based materials can be used as additives in perovskite layers to prevent bandgap widening, while facilitating perovskite crystal growth; thus, they are suitable for $FAPbI_3$ photoabsorbers in principle. However, BF_4^--based additives for narrow-bandgap $FAPbI_3$ photoabsorbers have not been developed. This is presumably because of the higher temperatures required for $FAPbI_3$ formation than that for other wide-bandgap perovskites, which likely changes the effects of BF_4-based additives from those for wide-bandgap perovskites. In this study, we verified the applicability of methylammonium tetrafluoroborate ($MABF_4$) as an additive in narrow-bandgap $FAPbI_3$ photoabsorbers for improving their PV performance primarily via the spontaneous modulation of the heterointerfaces between $FAPbI_3$ and carrier-transport materials, rather than through crystal growth facilitation. At the interface of the hole-transport material and $FAPbI_3$, $MABF_4$ addition effectively eliminates the surface defects in all $FAPbI_3$ components, even in the absence of BF_4^- anions over the heated $FAPbI_3$ surface, suggesting a defect-suppression mechanism, which differs from that observed in conventional ones. Moreover, at the interface of $FAPbI_3$ and the TiO_2 electron-transport material, the BF_4^--derived species, which likely includes decomposed BF_4^- anions owing to the high-temperature heating, spontaneously segregates upon deposition, thereby modulating the heterointerface. Furthermore, in addition to the carrier mobility ratio in $FAPbI_3$ (e^-:h^+ ≈ 7:3), time-resolved microwave conductivity

measurement revealed that BF_4 addition eliminates carrier traps at the heterointerfaces. Our findings provide insights into the promising $FAPbI_3$-based PSCs, offering a valuable tool for their further development.

1. Introduction

Perovskite solar cells (PSCs) have attracted global attention since their first demonstration of power conversion efficiency (PCE) of ~10% with an n-i-p standard structure[1, 2] and have undergone rapid development in the last decade. PSCs with a standard structure consist of multiple layers: transparent conductive glass/electron transport material (ETM)/perovskite photoabsorber/hole transport material (HTM)/metal electrode (e.g., fluorine-doped tin oxide (FTO) glass/TiO_2/perovskite/Spiro-OMeTAD/Au). Among PSC composites, perovskite photoabsorbers play an important role for achieving high performance.[3, 4] Perovskite crystals are represented by the ABX_3 structure, comprising organic cations, lead cations (Pb^{2+}), and halide anions at the *A*, *B*, and *X* sites, respectively. The modulation of perovskite crystal composites is a promising strategy for improving the photovoltaic (PV) performance of PSCs.

Among the perovskite composites, formamidine (FA)-lead-iodide ($FAPbI_3$) perovskite is promising because their bandgap is relatively close to the ideal single-cell bandgap (≈1.4 eV).[5-25] The perovskite crystal quality can be tuned by adding monoatomic ions, such as Cs^+ and Br^-, to the $FAPbI_3$ perovskite layer.[26-30] However, these additives increase the perovskite bandgap, thereby limiting the advantages of narrow-bandgap $FAPbI_3$. The addition of molecular ions can produce effects that cannot be achieved by the addition of monoatomic ions. The molecular tetrafluoroborate anion (BF_4^-) has an ionic radius (2.18 Å) close to that of iodine (2.20 Å) and can act as a substitute for I^- anions in the *X*-site perovskite.[31-46] Furthermore, it has been reported previously that the addition of BF_4^- does not increase the bandgap of wide-bandgap perovskites (e.g., $Cs_{0.2}FAPb(I_{0.8}Br_{0.2})_3$: bandgap ~1.62 eV).[33-46] Therefore, addition of BF_4-based materials into the $FAPbI_3$ perovskite is a promising strategy to retain its narrow bandgap while tuning its properties. However, effective BF_4^- addition to $FAPbI_3$ perovskites without Cs^+ and/or Br^- has not

yet been developed, which can be ascribed to the limited information on the relevant effects of BF_4^-.

The addition of BF_4^- to the perovskite layers has key effects on the bulk, and thus, this has been studied significantly. For example, BF_4^--based additives facilitate the crystal growth of wide-bandgap perovskites (e.g., $Cs_{0.2}FAPb(I_{0.8}Br_{0.2})_3$), enhancing their PV performance by exploiting the improved quality of the perovskite photoabsorber.[33-46] Meanwhile, since PSCs consist of multiple layers, the heterointerfaces between the perovskite photoabsorber and carrier-transport materials (CTMs, i.e., ETM and HTM) are expected to have a significant impact on PV performance.[47-51] Even though the effects of BF_4^- addition on PSCs based on wide-bandgap perovskite photoabsorbers have been extensively studied, the effects of BF_4^- addition in the narrow-bandgap $FAPbI_3$ layer especially on the heterointerfaces have seldom been investigated.

In this study, methylammonium (MA) BF_4 ($MABF_4$) was added to a narrow-bandgap $FAPbI_3$ perovskite to improve its PV performance while maintaining its narrow bandgap. To examine the effects of BF_4 anions, $MABF_4$ was employed as a representative BF_4^- additive because its counter cation (MA) is same as that of the co-additive of methylammonium chloride (MACl), a vital additive for practical $FAPbI_3$ crystallization.[7-12, 23, 52] $MABF_4$ addition effectively improved the PV performances of $FAPbI_3$-based PSCs primarily via enhancement of the heterointerfaces between the $FAPbI_3$ layer and CTMs, rather than facilitation of the crystal growth of the bulk perovskite (Figure 1). For the HTM/$FAPbI_3$ heterointerface, corresponding to outer surface of perovskite layer, $MABF_4$ addition effectively suppressed the defects of all the $FAPbI_3$ components presumably via a mechanism, which is different from conventional ones. Meanwhile, regarding the $FAPbI_3$/ETM heterointerface, which is underneath the $FAPbI_3$ layer, compositional depth analysis and time-resolved microwave conductivity (TRMC) measurements revealed the

segregation of BF_4-derived species in the $FAPbI_3$ layer at the $FAPbI_3$/ETM interface, which most likely suppressed carrier traps at the interface, leading to extremely long hole-lifetime in the $FAPbI_3$ layer. Therefore, the obtained insights regarding BF_4-based additives and their effects on narrow-bandgap $FAPbI_3$, which are different from those for wide-bandgap perovskites, will be a valuable guidance for further development of PSCs.

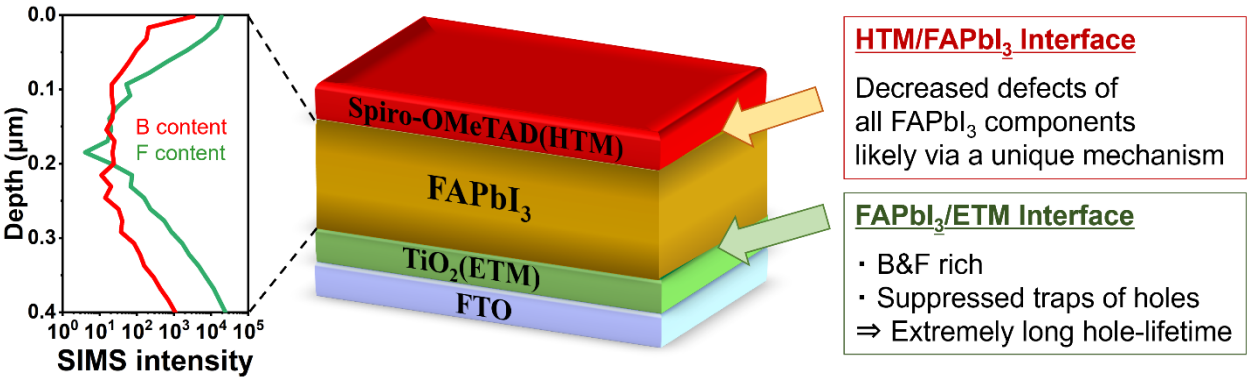

Figure 1. Schematic of $MABF_4$ addition to $FAPbI_3$ for heterointerface modulation

2. Experimental Section

$FAPbI_3$-based PSCs were fabricated using a conventional method[10, 18-20] with minor modifications (see Supporting Information (SI) for more details). A compact TiO_2 layer was deposited via spray pyrolysis of a titanium diisopropoxide bis(acetylacetate) ethanol solution over FTO at 450 °C, followed by mesoporous TiO_2 deposition via spin coating. Perovskite precursor solutions were prepared by dissolving 1.8 M $FAPbI_3$ powder, 0.72 mM MACl, and the desired amount of $MABF_4$ in a mixed solution of *N,N*-dimethylformamide and dimethyl sulfoxide (4:1, v/v). The perovskite layer was deposited by spin coating the precursor solution at 6000 rpm and 50 s and annealing at 150 °C for 10 min. During spin coating, chlorobenzene (1.0 mL) was added dropwise after 10 s of spinning. A passivation layer was deposited by spin coating a *n*-octylammonium iodide (OAI)

solution (15 mM) over the perovskite layer at 3000 rpm for 30 s and heating at 100 °C for 5 min.[53] [54] Subsequently, HTM was deposited by spin coating a mixture chlorobenzene solution containing spiro-OMeTAD,, 4-*tert*-butylpyridine, lithium bis(trifluoromethanesulfonyl)imide, and FK209 at 4000 rpm for 10 s. Finally, Au was deposited via evaporation.

3. Results and Discussion

The optical absorption spectra of the $FAPbI_3$ perovskite monolayer samples with and without $MABF_4$ were measured to investigate the bandgap with BF_4^- addition. Figure 2a shows the absorption spectra as a function of the $MABF_4$ addition. The $FAPbI_3$ without $MABF_4$ exhibited a bandgap of 1.54 eV. The bandgap was maintained with the addition of up to 5 mol% $MABF_4$, whereas it decreased slightly to 1.53 eV with the addition of 10 mol% $MABF_4$. Therefore, in contrast to Cs^+ and Br^- additives, the addition of $MABF_4$ to $FAPbI_3$ did not increase the bandgap rather slightly decreased.

According to previous studies on wide-bandgap perovskites, one of the roles of BF_4^--based additives is the facilitation of perovskite crystal growth. Accordingly, the crystal-growth properties of the $FAPbI_3$ perovskite layer were investigated. Figure S1 shows the X-ray diffraction (XRD) patterns of the perovskite layers with and without $MABF_4$. A slight change in the XRD peak at around 14°, corresponding to the (110) face was observed among the samples; no peak shifts were observed with up to 5 mol% $MABF_4$ addition, while a small peak shift from 13.94° to a slightly larger angle (13.96°) was observed with 10 mol% $MABF_4$ addition (Figure S1b). According to previous studies on the wide-bandgap perovskites, $Cs_{0.2}FA_{0.8}Pb(I_{0.8}Br_{0.2})_3$ for instance, the replacement of Br^- anions with BF_4^- anions afforded a shift in the XRD peak due to the substantially smaller ionic radius of the Br^- anion (1.96 Å)[3] compared to that of the BF_4^- anion

(2.18 Å).[45] The perovskite used in this study is composed of only I^- anions (i.e., $FAPbI_3$), which have an ion radius similar to that of BF_4^- (BF_4^-: 2.18 Å, I^-: 2.20 Å); therefore, minimal changes were observed in the XRD pattern upon $MABF_4$ addition. The slight shift in the XRD peak upon addition of 10 mol% $MABF_4$ can be ascribed to the incorporation of MA cations (2.70 Å) that are smaller than FA cations (2.79 Å). [55] In terms of δ phase $FAPbI_3$, which is inactive for the photoabsorber, the $MABF_4$ addition effectively suppress the formation of the δ phase $FAPbI_3$ (Figure S1c), which is consistent with the facilitated crystal growth of active $FAPbI_3$ as will be discussed hereafter.

Although a little changes were observed in the XRD patterns, the morphology varied considerably upon $MABF_4$ addition. The scanning electron microscopy (SEM) images of the perovskite layers with and without $MABF_4$ are shown in Figure 2b. The grain size of the perovskite increased with increasing $MABF_4$ content, indicating that the $MABF_4$ addition expedited the crystal growth of $FAPbI_3$. This crystal growth is mainly ascribed to the strong interaction between BF_4^- and the lead halide octahedron ($[PbX_6]^{4-}$) owing to the high electronegativity and strong electron affinity of BF_4^-.[45] Owing to these features, the nucleation of the perovskite crystals was impeded, which in turn expedited their crystal growth.[45] Larger crystal grains are advantageous for reducing carrier traps, which is beneficial for PV performance.

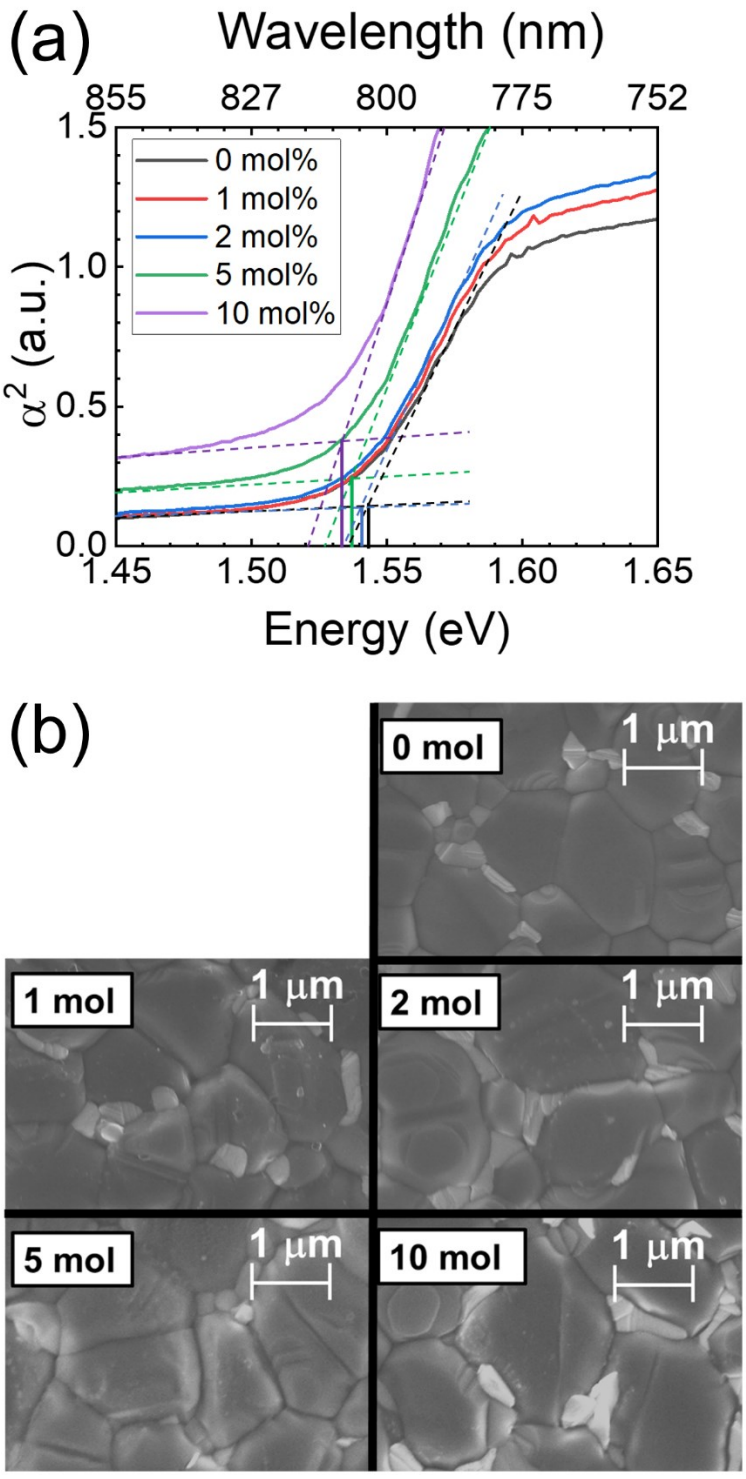

Figure 2. (a) UV–vis absorption spectra and bandgap with different BF_4^- addition amounts. (b) SEM top-view image of the perovskite films with different amounts of $MABF_4$.

$MABF_4$ addition facilitated crystal growth of the $FAPbI_3$ perovskite layer. However, the PV parameters of PSCs with $MABF_4$ addition describe another effect: the modulation of the heterointerfaces between the perovskite layer and CTMs. Figure 3 presents the PV parameters derived from the current density–voltage (J–V) curves of PSCs with and without $MABF_4$, indicating that optimal $MABF_4$ addition enhanced the PV performance. Figure 3a shows distribution of the power conversion efficiency (PCE) obtained under the backward scan. The average PCE under the backward scan (Table S1) increased from 20.0 ± 1.3% to 21.1 ± 0.9%, 21.6 ± 0.9%, and 21.3 ± 0.7% upon a $MABF_4$ addition of 1, 2, and 5 mol%, respectively. This PCE increases were mainly owing to the increase in the fill factors (FFs) from 0.70 ± 0.04 to 0.75 ± 0.02, 0.77 ± 0.03, and 0.75 ± 0.02, respectively (Figure S2 and Table S1). Similarly, in the champion cells (Table 1), the addition of 1, 2, and 5 mol% $MABF_4$ increased the PCE from 22.0% to 22.3%, 22.9%, and 22.9%, respectively, under the backward scan. The highest increase in PCE was attributed to the FF enhancement from 0.75 to 0.77, 0.79, and 0.78 with the addition of 1, 2, and 5 mol% $MABF_4$, respectively. Meanwhile, under the forward scan, $MABF_4$ addition decreased PCEs in the averages (Figure S3 and Table S1) and champion cells (Table 1) owing to a decrease in the open-circuit voltage (V_{oc}). In the champion cells, PCEs decreased from 20.5% without $MABF_4$ to 18.4% with 2 mol% $MABF_4$ owing to the decrease in V_{oc} from 1.12 to 1.03 V. Overall, for the J–V curves, the addition of up to 5 mol% $MABF_4$ enhanced the PCEs of PSCs in the backward scan, however, it also enlarged their hysteresis.

Quasi-steady-state PCEs (QSS-PCEs) were measured for the champion cells to investigate the practical enhancement of PCE upon $MABF_4$ addition. Figure 3c shows QSS-PCEs with and without $MABF_4$. The PSC without $MABF_4$ exhibited a QSS-PCE of 21.7%, which was similar to the value of the J–V curve under the backward scan. The addition of 1 and 2 mol% $MABF_4$

increased the QSS-PCE to 22.6% and 22.7%, respectively, which are also similar to the value in the J–V curves under the backward scan, indicating the PV performance enhancement by the $MABF_4$ addition. In contrast, the QSS-PCE of the PSC with 5 mol% $MABF_4$ showed an unstable trend and a lower value of 16.6% at 100 s. Similarly, a poor PV performance was determined from the external quantum efficiency (EQE) spectra of the sample with 5 mol% $MABF_4$ addition. Figure 3d shows the EQE spectra of PSCs with and without $MABF_4$. The J_{sc} in the J–V curves of the PSCs with 0 (26.0 mA cm^{-2}), 1 mol% (26.3 mA cm^{-2}), and 2 mol% (26.2 mA cm^{-2}) $MABF_4$ matched well with the integrated J_{sc} estimated from the EQE curves within 3% (25.2, 25.1, and 25.1 mA cm^{-2}, respectively). Meanwhile, the samples with 5 mol% $MABF_4$ achieved low EQE values leading to low integrated J_{sc} (23.3 mA cm^{-2}) despite the similar J_{sc} values in the J-V curve to those with 0, 1, and 2 mol% $MABF_4$, indicating that the sample with 5 mol% $MABF_4$ deviates from the linearity of the current–excitation intensity relationship.

Overall, the optimal $MABF_4$ addition (i.e., 1 and 2 mol% addition) enhanced PCE mainly owing to the increase in FF. However, this trend differs from the effects of conventional BF_4^--based additives for wide-bandgap perovskites, whereby enhanced PV performance was mainly attributed to the increase in V_{oc} owing to the enhanced quality of the perovskite photoabsorbers with facilitated crystal growth.[31-46] In addition to the facilitated crystal growth of $FAPbI_3$, in the present PSCs, other factors contributed to the enhanced PV performance upon addition of $MABF_4$ to the $FAPbI_3$ perovskite. Therefore, the modulation of the heterointerface between the $FAPbI_3$ perovskite and CTMs with $MABF_4$ addition and its primary contribution to the PV performance enhancement were examined in this study.

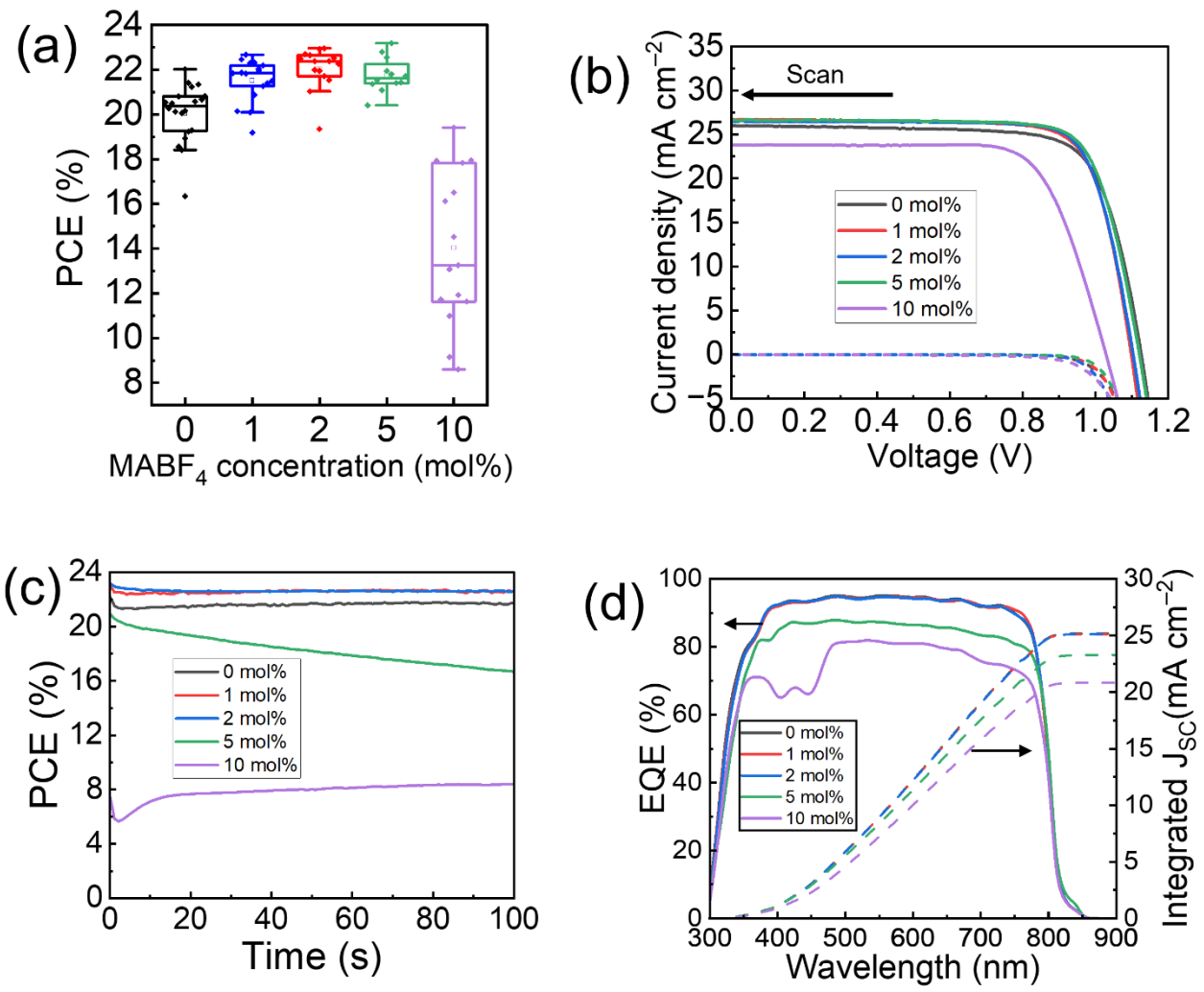

Figure 3. PV performance of PSCs with and without $MABF_4$: (a) distribution of PCEs in backward scan (corresponding PV parameters: Figure S2 , PV parameters in forward scan: Figure S3); (b) J-V curve with dark (dashed line) in backward scan (forward scan: Figure S4); (c) QSS-PCEs at 0.93, 0.92, 0.92, and 0.80 V for the samples with 0, 1, 2, 5, and 10 mol% $MABF_4$; and (d) EQE action spectra with integrated J_{sc} (dashed line).

Table 1. PV parameters of champion devices with 0, 1, 2, 5, and 10 mol% $MABF_4$

$MABF_4$ concentration (mol%)	Forward				Backward			
	J_{SC} (mA cm^{-2})	V_{OC} (V)	FF	PCE (%)	J_{SC} (mA cm^{-2})	V_{OC} (V)	FF	PCE (%)
0	26.1	1.12	0.70	20.5	26.0	1.13	0.75	22.0
1	26.3	1.07	0.69	19.5	26.3	1.10	0.77	22.3
2	26.2	1.03	0.68	18.4	26.2	1.10	0.79	22.9
5	26.2	1.05	0.66	18.1	26.2	1.12	0.78	22.9
10	25.3	0.87	0.33	7.2	23.8	1.03	0.73	17.9

Regarding heterointerface modulation, we first investigated the HTM/$FAPbI_3$ interface corresponding to the $FAPbI_3$ outer surface. Figures 4 and S5 present the X-ray photoelectron spectroscopy (XPS) results of samples with and without $MABF_4$. In the Pb 4f spectra (Figures 4a), peaks corresponding to Pb^{2+} (at 143 and 138 eV) and Pb^0 (i.e., the metallic state, at 141 and 137 eV) were observed. An increase in $MABF_4$ concentration led to a decrease in the intensity of the Pb^0 (metallic) peaks. Since Pb^0 acts as a defect and can cause electron leaking, its decrease presumably contributed to the enhancement of the observed PV performance. Figure S5a shows a slight high-energy shift of the Pb^{2+} peaks from 143.1 to 143.3 eV with the addition of $MABF_4$. The formation of anion defects from Pb weakens the coordination between Pb and halogens and thereby results in a low-energy shift. Therefore, the observed high-energy shift indicates that the defects of anion coordinating to Pb^{2+} were effectively eliminated by the added $MABF_4$, contributing to the observed improvement in PV performance.

Apart from Pb, XPS of the other perovskite composites (i.e., C, N, and I) did not exhibit any peak shifts (Figure S5b–d). However, their surface compositions also indicated mitigation of surface defects upon $MABF_4$ addition. The I/Pb composition ratios of the I anion are presented in Figure 4b. An increase in the added amount of $MABF_4$ from 0 to 10 mol% gradually increased the I/Pb ratios from 1.3 to 1.8, and consequently, decreased the difference between the experimental and theoretical values (3.0). This trend suggests that $MABF_4$ addition contributed to the decrease in the iodine defect density, which is consistent with the high-energy shift of the Pb^{2+} peaks with $MABF_4$ addition (Figure S5a).

Figures 4c and 4d present the experimental and theoretical composition ratios of C/Pb and N/Pb, respectively, for the A-site perovskite composites. Without $MABF_4$ addition, the measured C/Pb (0.3), N/Pb (0.3), and N/C (0.9) ratios differed significantly from their corresponding theoretical values of 1.0, 2.0, and 2.0, respectively. However, the addition of $MABF_4$ increased the C/Pb ratio from 0.2 to 0.4, approaching the theoretical value of 1.0, and raised the N/Pb ratio from 0.3 to 0.5, nearing the theoretical value of 2.0. These increases suggest a mitigation of the perovskite A-site cation defects. Figure 4e shows the experimental and theoretical N/C composition ratios. For FA, the experimental ratio is close to the theoretical value of 2.0, indicating that over the perovskite surface, the amount of FA exceeds that of MA, which originated from MACl and $MABF_4$. Notably, the addition of $MABF_4$ raised the N/C ratio from 0.9 to 1.5, approaching the theoretical value for FA (2.0) and surpassing that for MA (1.0). These results demonstrate that $MABF_4$ addition effectively suppressed the surface defects of FA on the $FAPbI_3$ surface. This decreased FA defect presumably contributed to the optical bandgap shift of $FAPbI_3$ to the slightly narrower one observed in Figure 2a, as estimated by a theoretical study[41]. Consequently, optimal $MABF_4$ addition reduced the defects generated from all the $FAPbI_3$

compositions, including FA cations, Pb^{2+} cations, and I^- halogens. This phenomenon is advantageous for both effective hole collection and prevention of electron leakage, leading to the enhancement of PV performance.

The perovskite surfaces were examined regarding BF_4 anion compositions to investigate their defect suppression mechanism, and the absence of BF_4 species on the perovskite surface was revealed. Figure S5e presents the XPS profile of F 1s; fluorine peaks were not observed with the addition of 1–5 mol% $MABF_4$, whereas the addition of 10 mol% $MABF_4$ resulted in a small peak at 684 eV. Figure S5f shows the XPS profile of B 1s; boron peaks (189 eV) were absent in the spectra of all samples. We here note that the peaks at 186 and 198 eV in Figure S5f derived from I 4s and Cl 2p, respectively, meaning that no boron was detected. Therefore, the BF_4 species most likely disappeared from the perovskite surface during the heating process of the perovskite layer. This trend differs from previously reported ones regarding other types of perovskites (e.g., $Cs_{0.2}FAPb(I_{0.8}Br_{0.2})_3$), which require lower heating temperatures around 373 K, more suitable for p-i-n inverse structured PSCs, compared to $FAPbI_3$ (423 K; mostly used in n-i-p structure PSCs as in the present study). Consequently, the disappearance of BF_4 species from the perovskite surface may be attributed to the high heating temperatures applied. Previous studies on BF_4 addition to wide-bandgap perovskites[39, 45] and a theoretical estimation for $FAPbI_3$ perovskite[41] revealed that co-existing BF_4 anions on the perovskite surface stabilize FA and/or MA cations due to the strong electronegativity of the BF_4 anion. Thus, according to the literatures, the presence of BF_4 on a perovskite surface is vital for achieving this effect.[39, 41, 45] However, in the present system, the BF_4 anions disappeared from the perovskite surface during the post-heating process, yet $MABF_4$ addition to $FAPbI_3$ effectively suppressed defect formation. Hence, the mechanism for defect

suppression in this study presumably differs from that observed in conventional cases of BF_4 addition.

To investigate the defect suppression mechanism in the present system and assess the defect formation mechanism of $FAPbI_3$, XPS analysis of samples with BF_4 addition subjected to heating for various durations was conducted (Figure S6 and S7). The sample without heating exhibited an F 1s peak at 683 eV (Figure S6), corresponding to BF_4. However, with only 1 min of heating, the F 1s peak disappeared, suggesting that the BF_4 anion either evaporated or migrated to the underside during the initial stage of heating. Consequently, BF_4 anions were absent from the perovskite surface for most of the heating duration, though this BF_4 addition was effective in preventing defect formation (Figure 4). Indeed, the ratios of other components on the perovskite surface remained almost steady after heating for 1 min (Figure S7). These results suggest that BF_4 addition primarily affects the formation of crystal nuclei at the initial stage of perovskite layer formation. Compared to ions in rigid bulky crystals, nucleated ions generally move more easily; in other words, the crystalline nuclei are prone to form defects. Therefore, the addition of $MABF_4$ presumably suppresses the formation of defect nuclei and, eventually, the overall defect formation on the $FAPbI_3$ perovskite surface. Such findings also imply that for achieving high-quality $FAPbI_3$, which requires relatively high-temperature heating, controlling the nucleus states and suppressing the formation of defective crystal nuclei can be essential.

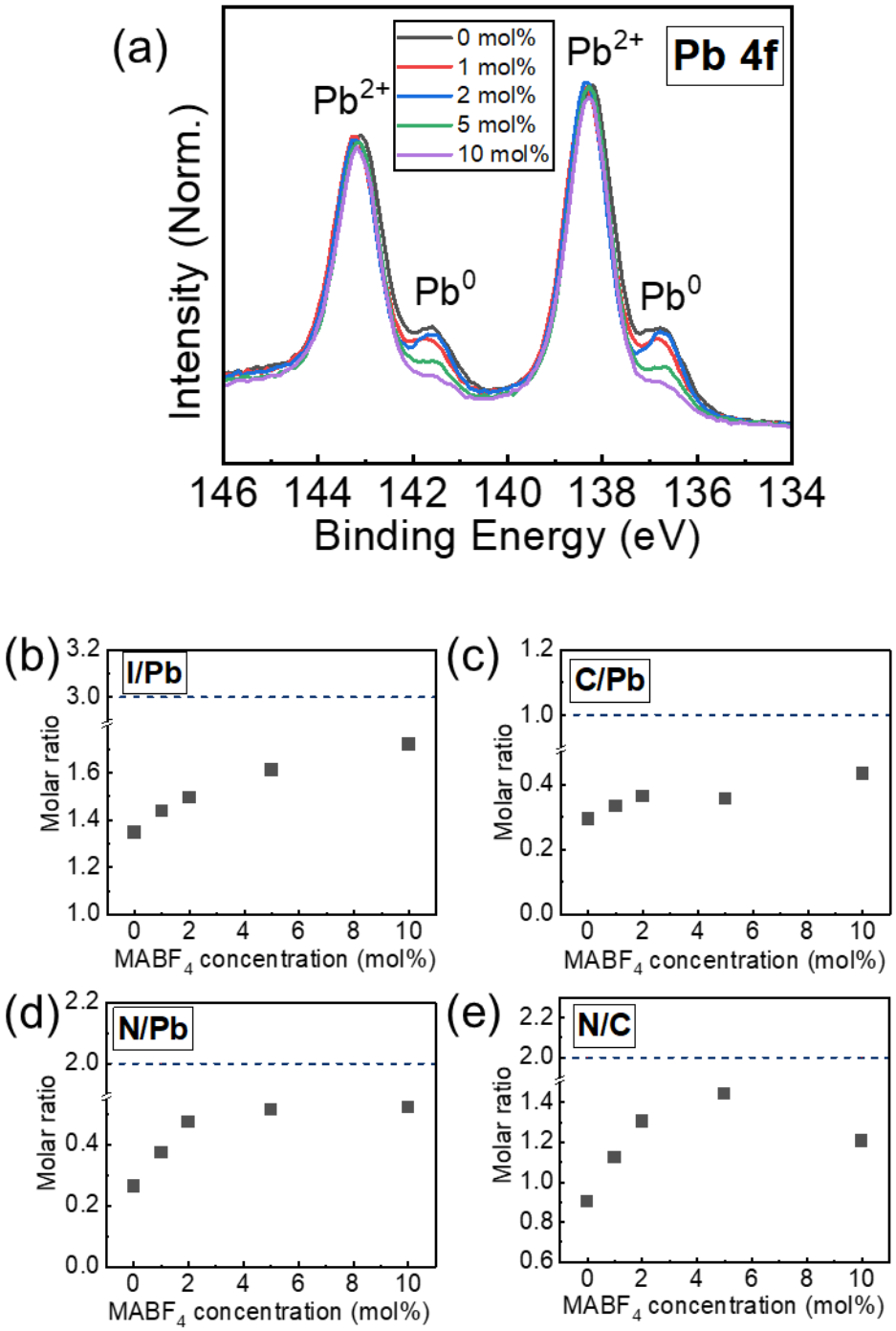

Figure 4. (a) XPS Pb 4f profile of the $FAPbI_3$ films with various amounts of $MABF_4$, estimated surface molar ratios of the samples (b) C/Pb, (c) N/Pb, (d) N/C, and (e) I/Pb (dashed line: theoretical values).

Apart from the HTM/$FAPbI_3$ interface, the effects of $MABF_4$ addition on the underlying $FAPbI_3$/ETM heterointerface were also investigated. To analyze the underlying $FAPbI_3$/ETM heterointerface, a compositional depth analysis was conducted. Figure 5 shows the secondary-ion mass spectrometry (SIMS) result of the samples with and without $MABF_4$. To detect F and B ions, SIMS analyses of the negative and positive ions were performed, respectively. The perovskite, TiO_2, and FTO regions were differentiated according to the Pb, Ti, and Sn concentrations at depths of 30 cycles (perovskite), 80 cycles (TiO_2), and 170 cycles (FTO) (see experimental section in SI for the determination of each regime). The negative ions in the sample without BF_4^- (Figures 5a) at a depth of 22 cycles exhibited a sharp increase and saturated F content, which might be ascribed to the F originating from FTO. However, the F component trend of the sample containing $MABF_4$ was different from that of the sample without $MABF_4$; unlike the sample without $MABF_4$, F was present in the perovskite bulk and exhibited compositional gradation. In the vicinity of the perovskite surface, an F signal (approximately 10000 counts) was detected. We here note that BF_4^- was absent in the outermost layer (a few nanometers depth) of the $FAPbI_3$ perovskite, as detected by XPS. In contrast, SIMS analysis detected BF_4^- species in $FAPbI_3$ perovskite surface, but SIMS is estimated to have a depth resolution of several tens of nanometers, much deeper than that of XPS. Furthermore, the F signal counts decreased from 1000 to 10 as the depth was increased from 0 to 10 cycles. Subsequently, it steeply increased from 10 and saturated at over 10000 counts at a depth of 10 cycles, which was shallower than that of the sample without $MABF_4$ addition and thus could not be attributed to FTO. Accordingly, $MABF_4$ addition led to F compositional gradation; high F concentrations were observed in the vicinity of the perovskite surface and the $FAPbI_3/TiO_2$ interface. The positive-ion SIMS results for B exhibited similar trends to those of F observed in

the negative-ion SIMS results. For the sample with $MABF_4$ addition, the B signal count decreased from 1000 to 20 as the depth increased from 0 to 20 cycles, and then sharply increased from 10 to 10,000 as the depth increased from 10 to 40 cycles; notably, large counts were obtained for samples with broad perovskite/TiO_2 interfaces. In contrast, the sample without $MABF_4$ addition exhibited a considerably weaker B signal than the sample with BF_4^-. Thus, both B and F were detected at the same depth (10 cycles) and exhibited similar trends, which could be attributed to BF_4^- anions. Further investigations were conducted by time-of-flight (ToF)-SIMS analyses, which can detect the depth profiles of molecular ions. Negative-ion detection mode, which sensitively detects ions that easily become negatively charged, was employed for the ToF-SIMS measurement to detect BF_4^- anions. Figure S8 shows the depth profiles of the samples with and without 2 mol% $MABF_4$. Although the presence of F ($M = 19$) was clearly observed, a little BF_4 ($M = 87$) was also detected. This result suggests that some of the BF_4 anions were decomposed, likely because of the relatively high-temperature heating of the $FAPbI_3$ layer in the deposition process. Figure S9 presents the integrated mass spectra corresponding to F ($M = 19$) and BF_4 ($M = 87$) anions at all depths of the $FAPbI_3$ layer, excluding the FTO regime (2–35 cycles in Figure S8). The integrated intensity of BF_4 in the $FAPbI_3$ sample with $MABF_4$ addition was clearly observed to be around 3 (Figure S9a), confirming the presence of BF_4 anion in the $FAPbI_3$ layer. Meanwhile, integrated intensity of F was approximately 40, ten-times larger (Figure S9b). Although the BF_4 should be easily become negative ions, the detected intensity was significantly smaller than F. Thus, the detected F was most likely derived from the fragmentation of the BF_4 anion and decomposed BF_4-based species. We here note that the integrated intensities of BF_4 and F in the $FAPbI_3$ sample without $MABF_4$ addition were negligible, and hence, the detected BF_4 and F were originated from $MABF_4$ addition. Therefore, the presence of BF_4^- in the $FAPbI_3$ layer was confirmed from the integrated mass

spectrum, but the decomposition of the BF_4^- in the $FAPbI_3$ layer was also suggested. Consequently, the species derived from the BF_4^- anions segregated in the vicinity of the surface of the perovskite layer and, notably, at the $FAPbI_3/TiO_2$ interface; the addition of $MABF_4$ to the $FAPbI_3$ photoabsorber spontaneously modulated the perovskite bulk composition and $FAPbI_3/TiO_2$ heterointerface. Although a fraction of the BF_4 anions most likely decomposed, the spontaneous modulation of the $FAPbI_3$/ETM heterointerface was beneficial in terms of carrier dynamics and stability against humidity as discussed later.

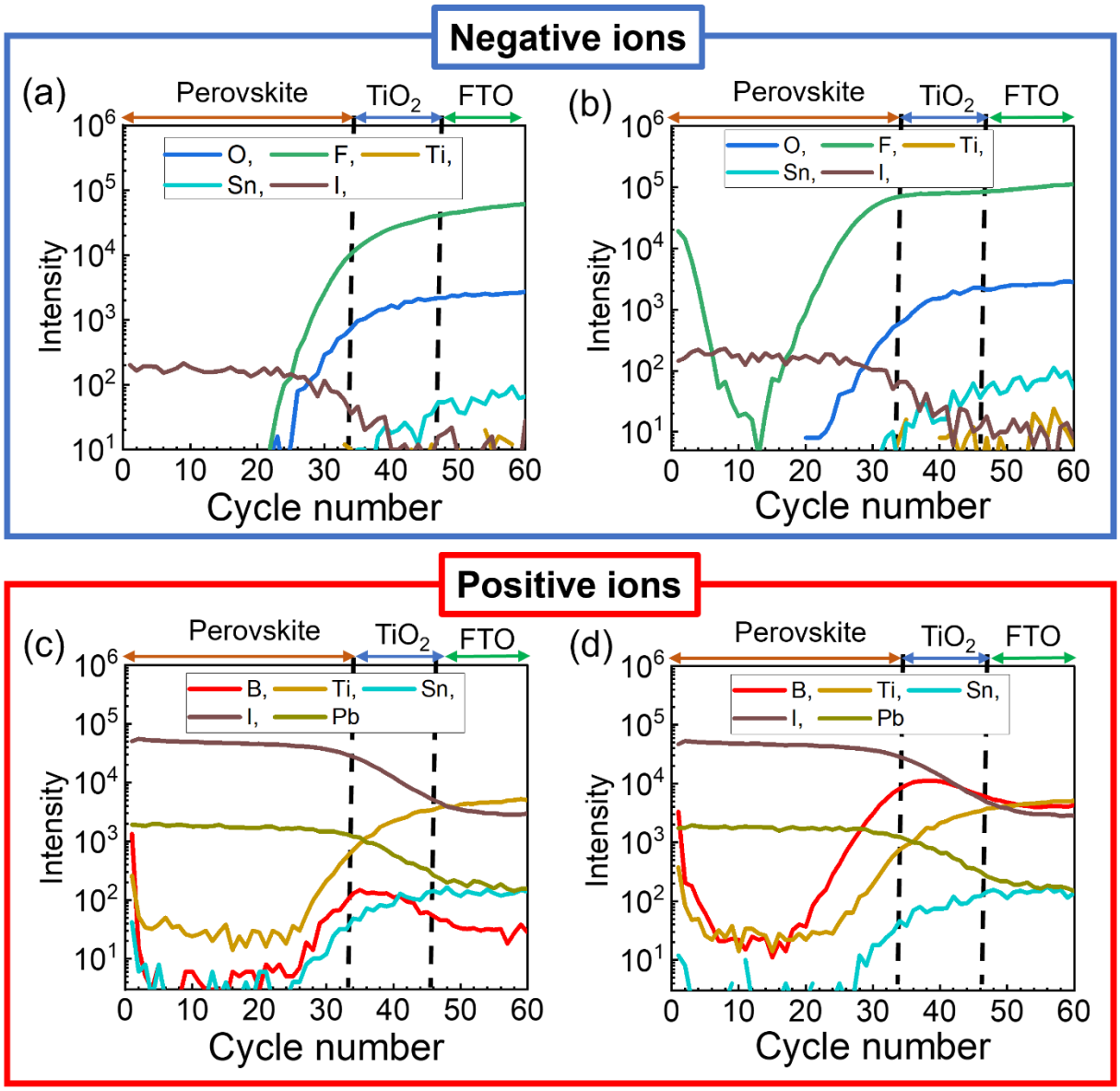

Figure 5. SIMS profiles and negative-ion defects: (a) without $MABF_4$, (b) with $MABF_4$ and positive ions, (c) without $MABF_4$, and (d) with $MABF_4$.

Examining the effects of this spontaneous modulation on the carrier dynamics is crucial to understand their contribution to the PV performance. TRMC measurements[19, 20, 56-62] are reportedly effective for investigating the carrier trapping ability of the heterointerface between the perovskite and CTMs in PSCs without removing CTMs. Because the carrier mobility in CTMs is significantly lower than that in perovskites, TRMC measurements are performed to determine the lifetime of the carriers remaining in the perovskite after carrier injection from the perovskite to a CTM. Thus, TRMC decay indicates changes in the electron trapping efficiency at the perovskite/CTM heterointerface (see SI for more details).

Prior to analyzing the CTM/$FAPbI_3$ heterointerfacial characteristics, TRMC measurements were conducted on the $FAPbI_3$ monolayer samples with and without $MABF_4$ addition. Figure S10a shows the TRMC decay of the $FAPbI_3$ monolayer samples with and without $MABF_4$ addition, and Figure 7a and Table S2 presents their TRMC lifetimes estimated via single exponential curve fitting. Regarding the TRMC measurements, a weak excitation of 0.6 nJ cm^{-2} per pulse was employed, sufficient to suppress the TRMC decay facilitated by high carrier concentration[20] (Figure S11). As the $MABF_4$ concentration increased from 0 to 1 mol%, the TRMC lifetime extended from 22.1 ± 0.3 to 54.1 ± 0.9 μs. A further increase in the $MABF_4$ concentration resulted in a slight decrease in the TRMC lifetime (e.g., with 2 and 10 mol% addition, the lifetime decreased to 43.0 ± 0.5 and 38.2 ± 0.4 μs, respectively); however, this shortened lifetime still surpassed that observed without $MABF_4$ addition. This extension of carrier lifetimes in the $FAPbI_3$ monolayer sample can be primely attributed to the improved interface of the $FAPbI_3$ perovskite and the quartz substrate as elucidated previously, in addition to the crystal growth facilitation observed in the SEM images (Figure 2b). Furthermore, the small decreases in the TRMC lifetimes upon excess

addition of $MABF_4$ suggest that excess $MABF_4$ addition can be detrimental to the quality of the perovskite layers perhaps due to the presence of decomposed BF_4 species.

The carrier injection characteristics and relative carrier mobilities were investigated via comparisons of the TRMC decay of the $FAPbI_3$ monolayer and CTM/$FAPbI_3$ bilayer samples within a short time scale (~1500 ns). Figures 6a and 6b present the TRMC signals of the samples with and without $MABF_4$ addition, respectively, for (i) $FAPbI_3$ perovskite monolayer, (ii) $FAPbI_3$/ETM bilayer, and (iii) HTM/$FAPbI_3$ bilayer samples. The TRMC signal intensities of the bilayer samples were normalized relative to that of the $FAPbI_3$ monolayer samples. Both types of samples with and without $MABF_4$ exhibited similar trends. The TRMC signals of the $FAPbI_3$ monolayer samples (black lines in Figures 6a and 6b) were almost steady within this time scale. The TRMC signal of the $FAPbI_3$/ETM bilayer (red lines in Figures 6a and b) gradually decreased up to approximately 500 ns and then became almost steady with an intensity of approximately 0.3 relative to that of the $FAPbI_3$ monolayer sample; therefore, the initial decay most likely represented the electron injection from $FAPbI_3$ to TiO_2 ETM. The HTM/$FAPbI_3$ bilayer sample (blue lines in Figures 6a and 6b) exhibited an initial signal intensity of 0.7 relative to that of the monolayer sample; subsequently, this signal intensity remained steady, suggesting that the hole injection from $FAPbI_3$ to the HTM was almost completed within the time resolution of the TRMC measurement. The estimated sum of the TRMC signal intensities of the $FAPbI_3$/ETM bilayer and that of the HTM/$FAPbI_3$ bilayers are also shown in Figures 6a and 6b as green dots. These results indicate that the sum of the TRMC intensities after the signal becomes steady (~500 ns) is approximately 1.0, which is the same as that of the $FAPbI_3$ monolayer sample. Therefore, this matching between the TRMC intensity of the monolayer and the sum value supports the aforementioned discussion; the initial signal decay shown by the $FAPbI_3$/ETM sample represents electron injection, and the

initially reduced signal intensity of the HTM/$FAPbI_3$ sample demonstrates that the hole injection is faster than the time resolution of the TRMC measurement. Thus, in the present system, the hole injection from $FAPbI_3$ to the HTM is significantly faster than the electron injection from $FAPbI_3$ to the ETM.

Such findings shed light on the carrier mobilities of the $FAPbI_3$ photoabsorber; the estimated carrier mobility ratio of $FAPbI_3$ between electrons (e^-) and holes (h^+) is approximately 7:3 for e^-:h^+. Although the mobilities of electrons and holes in perovskites are considered to be almost equal, it is revealed that in the case of the present $FAPbI_3$, the electron mobility is much higher than the hole mobility by approximately twofold.

To investigate the characteristics of the HTM/$FAPbI_3$ heterointerface, the TRMC signal decay of the HTM/$FAPbI_3$ bilayer samples was investigated (Figure 6c and Figure 7b). Hole injection was completed within the time resolution of the measurement, therefore, the TRMC decays of the HTM/$FAPbI_3$ bilayer samples represent the electron lifetime in the $FAPbI_3$ layer in the presence of the HTM/$FAPbI_3$ heterointerface ($\tau_{HTM/FAPbI3}$). The TRMC lifetime of the sample without $MABF_4$ addition was $\tau = 6.7 \pm 0.1$ μs, which is considerably shorter than that of the monolayer sample (Figure 7b and Table S2), indicating that the HTM/$FAPbI_3$ heterointerface acts as a significant carrier trap. The TRMC lifetimes remained almost unchanged with the addition of $MABF_4$ up to 2 mol% (1 mol%: $\tau = 8.7 \pm 0.1$ μs, 2 mol%: $\tau = 7.6 \pm 0.1$ μs), whereas they increased to 15.7 ± 0.2 μs and 12.3 ± 0.2 μs when 5 and 10 mol% of $MABF_4$ were added, respectively (Figure 7b and Table S2). However, even with $MABF_4$ addition, the TRMC decays of the HTM/$FAPbI_3$ bilayer samples were substantially shorter than those of the perovskite monolayer samples, strongly suggesting the formation of carrier traps at the HTM/$FAPbI_3$ heterointerface during the HTM deposition process. These carrier traps were presumably suppressed by $MABF_4$

as the TRMC lifetimes of the HTM/$FAPbI_3$ bilayer samples were extended. However, they remained even upon $MABF_4$ addition as represented by the shorter TRMC lifetimes of the HTM/$FAPbI_3$ samples compared to the corresponding $FAPbI_3$ monolayer samples.

Compared to the HTM/$FAPbI_3$ bilayer samples, the $FAPbI_3$/ETM bilayer samples exhibited a different trend. The TRMC signal of $FAPbI_3$/ETM in a short range (~1500 ns) is shown in Figure S10b. These TRMC decays represent both the electron injection from $FAPbI_3$ to ETM in the initial stage and the lifetime of the hole in $FAPbI_3$($\tau_{FAPbI3/ETM}$). Regarding the former characteristic, the TRMC lifetime attributed to electron injection ($\tau_{e\text{- }inject}$) was estimated and is presented in Figure 7c and Table S2 (see SI for estimation details). The $\tau_{e\text{- }inject}$ slightly increased from 86 ns to 220 ns with an increase in the $MABF_4$ concentration to 2 mol%. Further addition of $MABF_4$ to 5 and 10 mol% increased the $\tau_{e\text{- }inject}$ to 460 ns and 1566 ns, respectively. This increase in the $\tau_{e\text{- }inject}$ upon $MABF_4$ addition suggests that the accumulated BF_4-derived species around the $FAPbI_3/TiO_2$ interface may hamper electron injection from $FAPbI_3$ to TiO_2.

However, the accumulated BF_4 composite is presumably beneficial in suppressing carrier traps; after completion of the electron injection (i.e., after several μs), the TRMC decays correspond to the hole lifetimes in perovskite, while $MABF_4$ addition extended the TRMC lifetimes. Figure 6d and Figure 7d presents the TRMC decays of the $FAPbI_3$/ETM samples in a long-time range, and the hole-lifetimes corresponding to TRMC lifetime of these sample were estimated (Table S2). The $FAPbI_3$/ETM sample without $MABF_4$ addition exhibited a TRMC lifetime of $\tau = 221 \pm 12$ μs, which is considerably longer than that of the monolayer $FAPbI_3$ ($\tau = 22.1 \pm 0.3$ μs). This is presumably owing to the physically separated electrons and holes decreasing the recombination frequency, suggesting that the formed carrier traps at the $FAPbI_3$/ETM interface are substantially less than those at the HTM/$FAPbI_3$ interface ($\tau = 6.7 \pm 0.1$ μs). Meanwhile, with

an increase in $MABF_4$ addition from 0 to 1 and 2 mol%, the TRMC lifetime increased from 221 ± 12 to 266 ± 18 and 374 ± 32 μs, respectively. Further increase in $MABF_4$ addition to 10 mol% extended the TRMC lifetime to 516 ± 58 μs.

Consequently, optimal $MABF_4$ addition led to the extension of carrier lifetimes in the $FAPbI_3$ in the presence of heterointerfaces with CTMs, strongly suggesting suppression of carrier traps formation at the heterointerfaces. In particular, the hole lifetime in $FAPbI_3$ in the presence of the $FAPbI_3$/ETM heterointerface could be extended up to 516 ± 58 μs, which is extremely long. Thus, the decreased carrier traps presumably contributed to the enhancement of PV performance. However, excess $MABF_4$ addition inhibited electron injection from the $FAPbI_3$ to the TiO_2 ETM, which is considerably slower ($k_{e\text{- inject}} \sim 1.2 \times 10^7\ s^{-1}$) compared to hole injection from $FAPbI_3$ to Spiro-OMeTAD HTM ($k_{e\text{- inject}} > 5 \times 10^7\ s^{-1}$). Hence, this prevention of electron injection with excess $MABF_4$ addition could cause carrier accumulation at the heterointerface and might explain the observed QSS-PCE and EQE spectra of the PSCs with 5 mol% $MABF_4$.

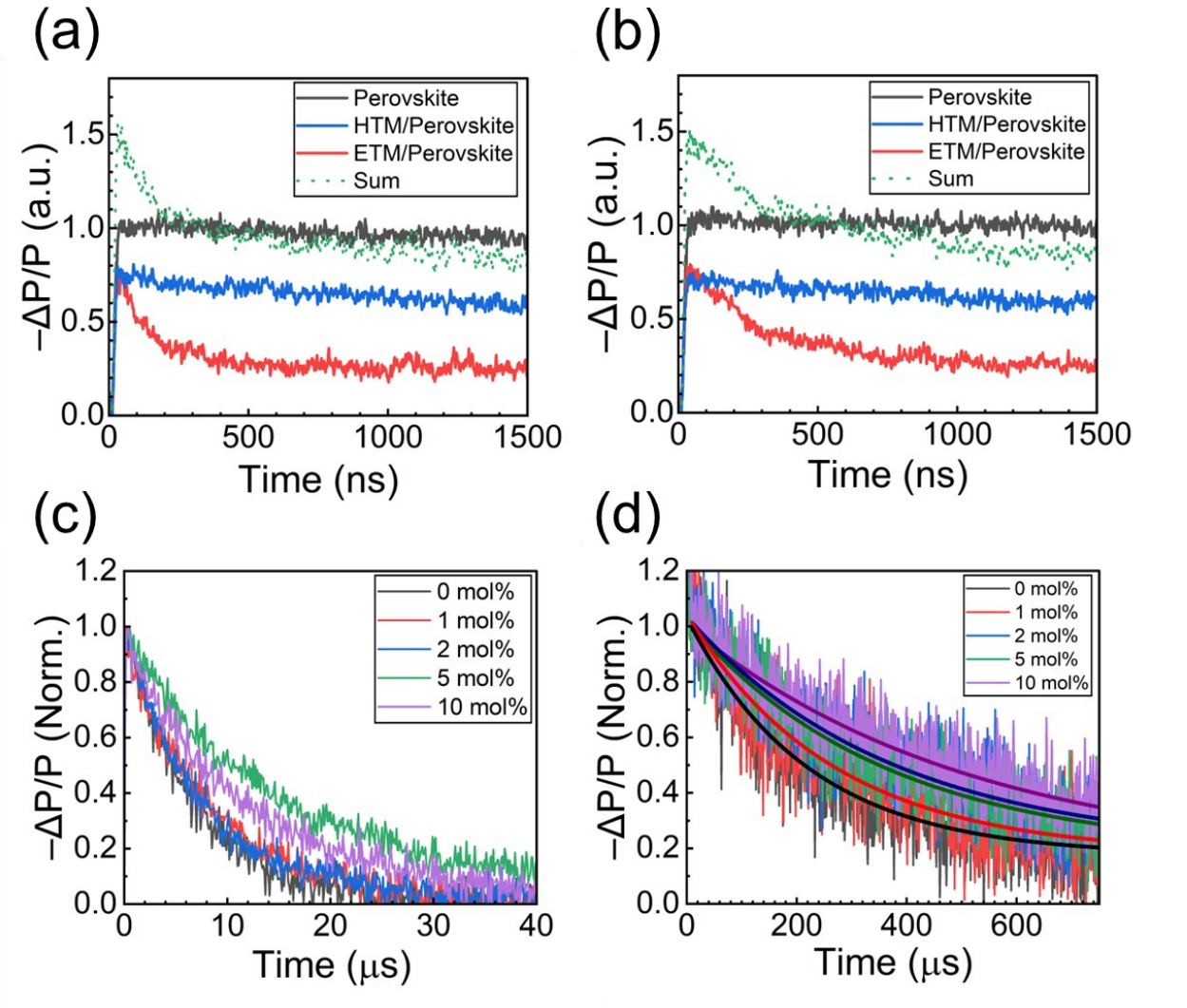

Figure 6. TRMC signal of the intensity of the monolayer and bilayer with a $MABF_4$ concentration of (a) 0 mol% and (b) 2 mol%. TRMC signal of the (c) HTM/$FAPbI_3$ and (d) $FAPbI_3$/ETM bilayers in a long range (short range: Figure S10b) with their corresponding fitting curves.

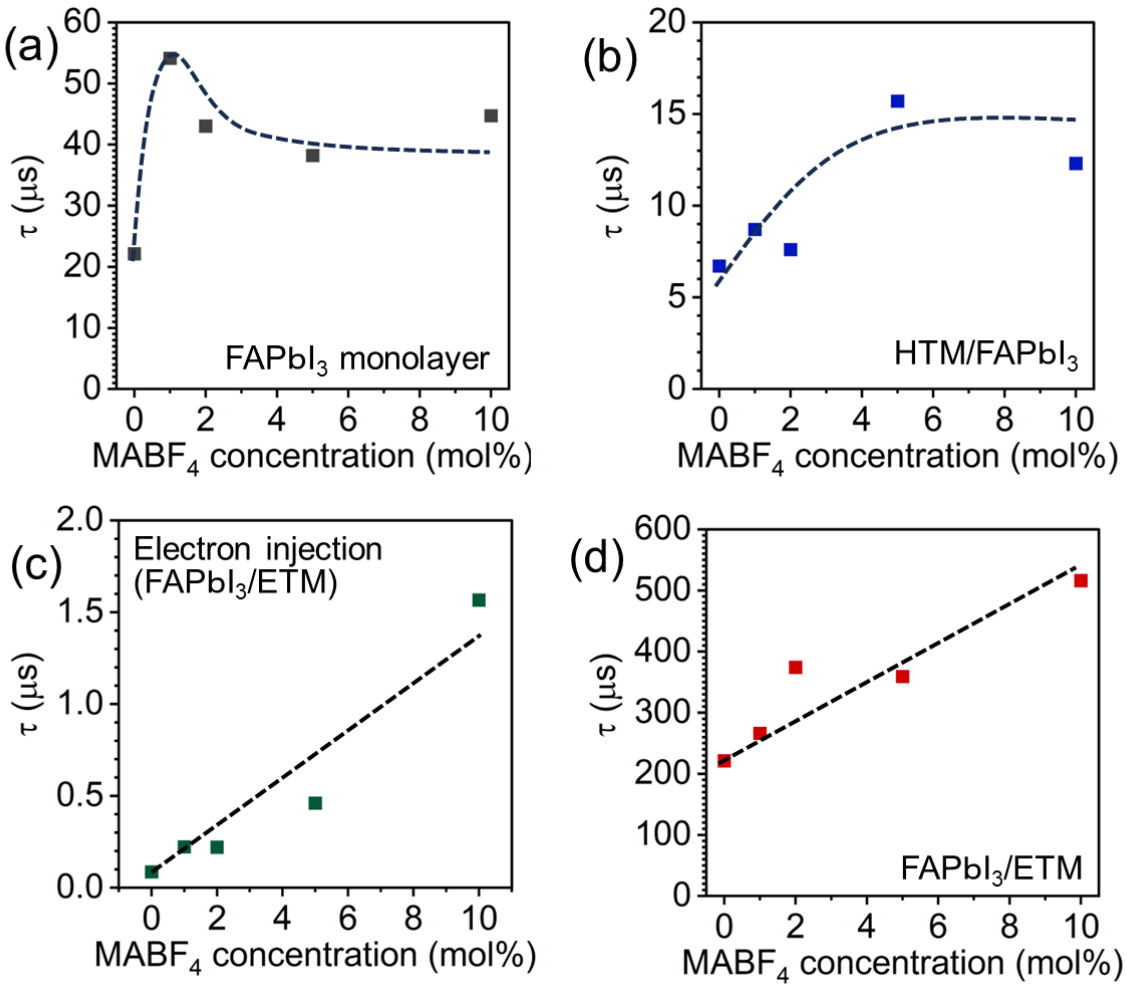

Figure 7. Averaged TRMC lifetimes of (a) $FAPbI_3$ monolayer samples, (b) HTM/$FAPbI_3$ bilayer samples, (c) $FAPbI_3$/ETM bilayer samples attributed to electron injection, (d) $FAPbI_3$/ETM bilayer samples after the electron injection

The addition of fluorinated components renders a material hydrophobic; therefore, the effects of $MABF_4$ addition on the PSC stability against humidity were investigated. Figure S12 shows the results of the stability tests conducted under humidity (303 K (30 ℃), 50% relative humidity). Initially, the PCE of the sample without $MABF_4$ decreased to ~40% after 1500 h. In contrast, the addition of the optimal amount of $MABF_4$ resulted in considerable moisture resistance with over

85% of the initial PCE maintained after 1500 h. Previous studies on the BF_4^- additive reported its effect on the surface hydrophobicity of the perovskite layer and its stability against humidity. However, in our study, the contact-angle measurements of the perovskite surfaces performed using water droplets indicated that BF_4^- addition did not increase the hydrophobicity of the perovskite surfaces for both cases with and without OAI passivation (Figure S13). Meanwhile, the SIMS results indicated that species derived from BF_4^- anions were incorporated into the perovskite layer, although part of the BF_4^- anions was most likely decomposed. Fluorinated moieties are known for their hydrophobicity,[63-65] thus, the BF_4^- anion species even partly decomposed render the perovskite bulk hydrophobic, and thereby, its stability against humidity was improved. Consequently, $MABF_4$ addition into $FAPbI_3$ is advantageous for improving the long-term stability of the devices against humidity owing to the presence of BF_4-derived species in the $FAPbI_3$ layer.

Conclusions

In this study, we revealed that although the combination of narrow-bandgap $FAPbI_3$ and BF_4-based additives, which can retain the narrow-bandgap, is promising, the effects of the additive on narrow-bandgap perovskites differ compared to those of wide-bandgap perovskites. Unlike conventional BF_4-based additives that primarily promote the crystal growth of wide-bandgap perovskites, the primary function of the $MABF_4$ additive in the $FAPbI_3$ photoabsorber is most likely the spontaneous modulation of the heterointerfaces between $FAPbI_3$ and the CTM. (Figure 1)

Although SEM images reveal that the addition of $MABF_4$ promoted $FAPbI_3$ crystal growth, the PV performance of the PSCs with the optimal amount of $MABF_4$ did not show V_{oc} enhancement, unlike in conventional BF_4 addition. Instead, the proposed approach increased the

FF values and, thereby, enhanced the PCEs, which is consistent with the role of spontaneous heterointerface modulation.

Regarding the outer perovskite surface corresponding to the HTM/$FAPbI_3$ heterointerface, XPS measurements indicate that the defects of all perovskite composites (i.e., C, N, Pb, and I) decreased on the addition of $MABF_4$. For surface defect suppression using BF_4-based additives, although the presence of the BF_4^- anion on the perovskite surface is vital for wide-bandgap perovskites, as shown by previous studies[39, 41, 45], the present results reveal that BF_4^- anion was absent on the $FAPbI_3$ surface during most of the duration for heating, suggesting a non-conventional defect suppression mechanism and provoking the importance of controlling $FAPbI_3$ nucleation.

Meanwhile, compositional depth analysis using SIMS revealed that the BF_4^- anions segregated at the $FAPbI_3$/ETM interface during deposition, although some of the BF_4^- anions were decomposed. TRMC measurements revealed the roles of the spontaneously modulated interfaces in addition to revealing the carrier mobility relationship of $FAPbI_3$: The carrier mobility ratio of $FAPbI_3$ between electrons (e^-) and holes (h^+) was 7:3, and the electron mobility in $FAPbI_3$ was substantially higher than that of the holes. Further, optimized $MABF_4$ addition effectively extended the carrier lifetimes in the presence of the heterointerfaces, and $MABF_4$ addition extended the hole lifetime of the $FAPbI_3$ photoabsorber in the presence of a $FAPbI_3/TiO_2$ heterointerface up to 516 ± 58 μs, which is extremely long. Thus, the improved heterointerfaces presumably contributed to the enhanced PV performance. (Figure 1) Furthermore, $MABF_4$ addition improved PSC stability against humidity presumably owing to the resulting hydrophobicity of the $FAPbI_3$ bulk upon the incorporation of BF_4^- species.

The promising combination of the narrow-bandgap $FAPbI_3$ and BF_4-based additives and identification of their roles in spontaneous heterointerface modulation will aid the further development of PSCs.

Supporting Information Available

Brief statement in nonsentence format listing the contents of the material supplied as Supporting Information

Author Contributions

Daisuke Kubota: Investigation, Resources, Formal analysis, Writing – original draft, Writing – review & editing, **Ryuzi Katoh:** Investigation, Formal analysis, Writing – review & editing, **Hiroyuki Kanda:** Writing – review & editing, **Hiroyuki Yaguchi:** Writing – review & editing, **Takurou N. Murakami:** Funding acquisition, Writing – review & editing, **Naoyuki Nishimura:** Supervision, Conceptualization, Project administration, Investigation, Resources, Formal analysis, Writing – review & editing**.**

Notes

There are no conflicts to declare.

Acknowledgement

This article is based on results obtained from the project JPNP21016, commissioned by the New Energy and Industrial Technology Development Organization (NEDO).

Abbreviations

CTM, carrier-transport material; ETM, electron transport material; EQE, external quantum efficiency; FA, formamidium; FTO, fluorine-doped tin oxide; FF, fill factor; MA, methylammonium; PCE, power conversion efficiency; PSC, perovskite solar cell; PV, photovoltaic; SIMS, secondary-ion mass spectrometry; TRMC, time-resolved microwave conductivity; XPS, X-ray photoelectron spectroscopy.

References

(1) Lee, M. M.; Teuscher, J.; Miyasaka, T.; Murakami, T. N.; Snaith, H. J. Efficient Hybrid Solar Cells Based on Meso-Superstructured Organometal Halide Perovskites. *Science* **2012**, *338*, 643-647.
(2) Kim, H. S.; Lee, C. R.; Im, J. H.; Lee, K. B.; Moehl, T.; Marchioro, A.; Moon, S. J.; Humphry-Baker, R.; Yum, J. H.; Moser, J. E.; et al. Lead Iodide Perovskite Sensitized All-Solid-State Submicron Thin Film Mesoscopic Solar Cell with Efficiency Exceeding 9%. *Sci Rep* **2012**, *2*, 591.
(3) Kim, J. Y.; Lee, J. W.; Jung, H. S.; Shin, H.; Park, N. G. High-Efficiency Perovskite Solar Cells. *Chem Rev* **2020**, *120*, 7867-7918.
(4) Bati, A. S. R.; Zhong, Y. L.; Burn, P. L.; Nazeeruddin, M. K.; Shaw, P. E.; Batmunkh, M. Next-Generation Applications for Integrated Perovskite Solar Cells. *Communications Materials* **2023**, *4*, 2.
(5) Koh, T. M.; Fu, K.; Fang, Y.; Chen, S.; Sum, T. C.; Mathews, N.; Mhaisalkar, S. G.; Boix, P. P.; Baikie, T. Formamidinium-Containing Metal-Halide: An Alternative Material for Near-IR Absorption Perovskite Solar Cells. *J. Phys. Chem. C* **2013**, *118*, 16458-16462.
(6) Han, Q.; Bae, S. H.; Sun, P.; Hsieh, Y. T.; Yang, Y. M.; Rim, Y. S.; Zhao, H.; Chen, Q.; Shi, W.; Li, G.; et al. Single Crystal Formamidinium Lead Iodide (FAPbI3): Insight into the Structural, Optical, and Electrical Properties. *Adv. Mater.* **2016**, *28*, 2253-2258.

(7) Wang, Z.; Zhou, Y.; Pang, S.; Xiao, Z.; Zhang, J.; Chai, W.; Xu, H.; Liu, Z.; Padture, N. P.; Cui, G. Additive-Modulated Evolution of HC(NH2)2PbI3 Black Polymorph for Mesoscopic Perovskite Solar Cells. *Chem. Mater.* **2015**, *27*, 7149-7155.
(8) Xie, F.; Chen, C.-C.; Wu, Y.; Li, X.; Cai, M.; Liu, X.; Yang, X.; Han, L. Vertical Recrystallization for Highly Efficient and Stable Formamidinium-Based Inverted-Structure Perovskite Solar Cells. *Ener. Environ. Sci.* **2017**, *10*, 1942-1949.
(9) Kim, M.; Kim, G.-H.; Lee, T. K.; Choi, I. W.; Choi, H. W.; Jo, Y.; Yoon, Y. J.; Kim, J. W.; Lee, J.; Huh, D.; et al. Methylammonium Chloride Induces Intermediate Phase Stabilization for Efficient Perovskite Solar Cells. *Joule* **2019**, *3*, 2179-2192.
(10) Jeong, J.; Kim, M.; Seo, J.; Lu, H.; Ahlawat, P.; Mishra, A.; Yang, Y.; Hope, M. A.; Eickemeyer, F. T.; Kim, M.; et al. Pseudo-Halide Anion Engineering for alpha-FAPbI3 Perovskite Solar Cells. *Nature* **2021**, *592*, 381-385.
(11) Bi, L.; Fu, Q.; Zeng, Z.; Wang, Y.; Lin, F. R.; Cheng, Y.; Yip, H. L.; Tsang, S. W.; Jen, A. K. Deciphering the Roles of MA-Based Volatile Additives for alpha-FAPbI3 to Enable Efficient Inverted Perovskite Solar Cells. *J. Am. Chem. Soc.* **2023**, *145*, 5920-5929. DOI: 10.1021/jacs.2c13566
(12) Min, H.; Kim, M.; Lee, S. U.; Kim, H.; Kim, G.; Choi, K.; Lee, J. H.; Seok, S. I. Efficient, Stable Solar Cells by Using Inherent Bandgap of alpha-Phase Formamidinium Lead Iodide. *Science* **2019**, *366*, 749-753.
(13) Choi, E.; Lee, J. W.; Anaya, M.; Mirabelli, A.; Shim, H.; Strzalka, J.; Lim, J.; Yun, S.; Dubajic, M.; Lim, J.; et al. Synergetic Effect of Aluminum Oxide and Organic Halide Salts on Two‐Dimensional Perovskite Layer Formation and Stability Enhancement of Perovskite Solar Cells. *Adv. Ener. Mater.* **2023**, *13*, 2301717.
(14) Elmestekawy, K. A.; Gallant, B. M.; Wright, A. D.; Holzhey, P.; Noel, N. K.; Johnston, M. B.; Snaith, H. J.; Herz, L. M. Photovoltaic Performance of FAPbI3 Perovskite Is Hampered by Intrinsic Quantum Confinement. *ACS Ener. Lett.* **2023**, *8*, 2543-2551.
(15) Huang, X.; Cao, F.; Zhan, S.; Feng, Q.; Zhu, M.; Su, Z.; Gao, X.; Yin, J.; Li, J.; Zheng, N.; et al. Solvent Racing Crystallization: Low-Solvation Dispersion Cosolvents for High-Quality Halide Perovskites in Photovoltaics. *Joule* **2023**, *7*, 1556-1573.
(16) Ge, J.; Chen, R.; Ma, Y.; Wang, Y.; Hu, Y.; Zhang, L.; Li, F.; Ma, X.; Tsang, S. W.; You, J.; et al. Kinetics Controlled Perovskite Crystallization for High Performance Solar Cells. *Angew. Chem. Int. Ed.* **2024**, *63*, e202319282.
(17) Park, K.; Tan, S.; Kodalle, T.; Lee, D. K.; Abdelsamie, M.; Park, J. S.; Lee, J. H.; Jung, S. K.; Ko, J. H.; Park, N. G.; et al. Atmospheric Humidity Underlies Irreproducibility of Formamidinium Lead Iodide Perovskites. *Adv. Mater.* **2024**, *36*, e2307265.
(18) Nishimura, N.; Mathew, S.; Murakami, T. N. Suppressing Hydrogen Bonds and Controlling Surface Dipole: Effective Passivation for Hydrophobic Perovskite Photoabsorber Layers in Solar Cells. *New. J. Chem.* **2023**, *47*, 4197-4201.
(19) Nishimura, N.; Tachibana, H.; Katoh, R.; Kanda, H.; Murakami, T. N. Archetype-Cation-Based Room-Temperature Ionic Liquid: Aliphatic Primary Ammonium Bis(trifluoromethylsulfonyl)imide as a Highly Functional Additive for a Hole Transport Material in Perovskite Solar Cells. *ACS Appl. Mater. Interfaces* **2023**, *15*, 44859-44866.
(20) Nishimura, N.; Behera, R. K.; Katoh, R.; Kanda, H.; Murakami, T. N.; Matsuzaki, H. Unveiled Effects of Methylammonium Chloride Additives on Formamidinium Lead Halide: Expediting Carrier Injection from the Photoabsorber to Carrier Transport Layers through

Spontaneously Modulated Heterointerfaces in Perovskite Solar Cells. *J. Mater. Chem. C* **2024**, *12*, 9130–9138.
(21) Yoo, J. W.; Noh, E.; Jang, J.; Lee, K. S.; Byeon, J.; Choi, M.; Im, J.; Seok, S. I. R4N+ and Cl− Stabilized α-Formamidinium Lead Triiodide and Efficient Bar-Coated Mini-Modules. *Joule* **2023**, *7*, 797-809.
(22) Huang, K.; Chang, L.; Hou, Y.; Ji, W.; Trần‐Phú, T.; Bui, A. D.; Mayon, A. O.; Wang, W.; Lem, O. L. C.; Nguyen, D. T.; et al. Universal Strategy with Structural and Chemical Crosslinking Interface for Efficient and Stable Perovskite Solar Cells. *Adv. Ener. Mater.* **2024**, 14, 2304073.
(23) Park, J.; Kim, J.; Yun, H. S.; Paik, M. J.; Noh, E.; Mun, H. J.; Kim, M. G.; Shin, T. J.; Seok, S. I. Controlled Growth of Perovskite Layers with Volatile Alkylammonium Chlorides. *Nature* **2023**, *616*, 724-730.
(24) Feng, F.; Guan, Y.; Liu, F.; Wu, C.; Su, H.; Wang, B.; Zhang, X.; Liang, Y.; Cai, S.; Zhang, Y.; et al. Efficient Additive-Free FAPbI3 Perovskite Solar Cells Achieved by Promoting Homogeneity. *J. Mater. Chem. C* **2024**, *12*, 3410-3417.
(25) Chen, Y.; Li, B.; Ye, Y.; Zhang, X.; Wang, B.; Fan, H.; Yuliarto, B.; Osman, S. M.; Yamauchi, Y.; Yin, Y. Stable FAPbI3 Perovskite Solar Cells via Alkylammonium Chloride-Mediated Crystallization Control. *ACS Appl. Mater. Interfaces* **2024**, *16*, 28402-28408.
(26) Li, Z.; Yang, M.; Park, J.-S.; Wei, S.-H.; Berry, J. J.; Zhu, K. Stabilizing Perovskite Structures by Tuning Tolerance Factor: Formation of Formamidinium and Cesium Lead Iodide Solid-State Alloys. *Chem. Mater.* **2015**, *28*, 284-292.
(27) Saliba, M.; Matsui, T.; Seo, J. Y.; Domanski, K.; Correa-Baena, J. P.; Nazeeruddin, M. K.; Zakeeruddin, S. M.; Tress, W.; Abate, A.; Hagfeldt, A.; et al. Cesium-containing Triple Cation Perovskite Solar Cells: Improved Stability, Reproducibility and High Efficiency. *Ener. Environ. Sci.* **2016**, *9*, 1989-1997.
(28) Saliba, M.; Matsui, T.; Domanski, K.; Seo, J. Y.; Ummadisingu, A.; Zakeeruddin, S. M.; Correa-Baena, J. P.; Tress, W. R.; Abate, A.; Hagfeldt, A.; et al. Incorporation of Rubidium Cations into Perovskite Solar Cells Improves Photovoltaic Performance. *Science* **2016**, *354*, 206-209.
(29) Kanda, H.; Shibayama, N.; Huckaba, A. J.; Lee, Y.; Paek, S.; Klipfel, N.; Roldán-Carmona, C.; Queloz, V. I. E.; Grancini, G.; Zhang, Y.; et al. Band-Bending Induced Passivation: High Performance and Stable Perovskite Solar Cells Using a Perhydropoly(silazane) Precursor. *Ener. Environ. Science* **2020**, *13*, 1222-1230.
(30) Lintangpradipto, M. N.; Zhu, H.; Shao, B.; Mir, W. J.; Gutiérrez-Arzaluz, L.; Turedi, B.; Abulikemu, M.; Mohammed, O. F.; Bakr, O. M. Single-Crystal Methylammonium-Free Perovskite Solar Cells with Efficiencies Exceeding 24% and High Thermal Stability. *ACS Ener. Lett.* **2023**, *8*, 4915-4922.
(31) Nagane, S.; Bansode, U.; Game, O.; Chhatre, S.; Ogale, S. CH3NH3PbI3-xBF4x: Molecular Ion Substituted Hybrid Perovskite. *Chem. Commun.* **2014**, *50*, 9741-9744.
(32) Nagane, S.; Ogale, S. CH3NH3PbBF4(3) and C4H9NH3(2)PbBF4(4) Family of 3D and 2D Perovskites without and with Iodide and Bromide Ions Substitution. *J. Phys. Chem. Lett.* **2016**, *7*, 4757-4762.
(33) Chen, J.; Rong, Y.; Mei, A.; Xiong, Y.; Liu, T.; Sheng, Y.; Jiang, P.; Hong, L.; Guan, Y.; Zhu, X.; et al. Hole‐Conductor‐Free Fully Printable Mesoscopic Solar Cell with Mixed‐Anion Perovskite CH3NH3PbI(3−x)(BF4)x. *Adv. Ener. Mater.* **2015**, *6*, 1502009.

(34) Bai, S.; Da, P.; Li, C.; Wang, Z.; Yuan, Z.; Fu, F.; Kawecki, M.; Liu, X.; Sakai, N.; Wang, J. T.; et al. Planar Perovskite Solar Cells with Long-Term Stability Using Ionic Liquid Additives. *Nature* **2019**, *571*, 245-250.
(35) Noel, N. K.; Habisreutinger, S. N.; Wenger, B.; Lin, Y. H.; Zhang, F.; Patel, J. B.; Kahn, A.; Johnston, M. B.; Snaith, H. J. Elucidating the Role of a Tetrafluoroborate‐Based Ionic Liquid at the n‐Type Oxide/Perovskite Interface. *Adv. Ener. Mater.* **2019**, *10*, 1903231.
(36) Zhang, J.; Wu, S.; Liu, T.; Zhu, Z.; Jen, A. K. Y. Boosting Photovoltaic Performance for Lead Halide Perovskites Solar Cells with BF4− Anion Substitutions. *Adv. Funct. Mater.* **2019**, *29*, 1808833.
(37) Lin, Y. H.; Sakai, N.; Da, P.; Wu, J.; Sansom, H. C.; Ramadan, A. J.; Mahesh, S.; Liu, J.; Oliver, R. D. J.; Lim, J.; et al. A Piperidinium Salt Stabilizes Efficient Metal-Halide Perovskite Solar Cells. *Science* **2020**, *369*, 96-102.
(38) Li, D.; Huang, Y.; Wang, G.; Lian, Q.; Shi, R.; Zhang, L.; Wang, X.; Gao, F.; Kong, W.; Xu, B.; et al. Boosting the Performance of MA-free Inverted Perovskite Solar Cells via Multifunctional Ion Liquid. *J. Mater. Chem. A* **2021**, *9*, 12746-12754.
(39) Nagane, S.; Macpherson, S.; Hope, M. A.; Kubicki, D. J.; Li, W.; Verma, S. D.; Ferrer Orri, J.; Chiang, Y. H.; MacManus-Driscoll, J. L.; Grey, C. P.; et al. Tetrafluoroborate-Induced Reduction in Defect Density in Hybrid Perovskites through Halide Management. *Adv. Mater.* **2021**, *33*, e2102462.
(40) Zhang, Z.; Guo, T.; Yuan, H.; Yu, L.; Zhao, R.; Deng, Z.; Zhang, J.; Liu, X.; Hu, Z.; Zhu, Y. Reconstruction of the (EMIm)(x)MA(1-x)Pb[(BF(4))(x)I(1-x)](3) Interlayer for Efficient and Stable Perovskite Solar Cells. *ACS Appl. Mater. Interfaces* **2021**, *13*, 727-733. DOI: 10.1021/acsami.0c19784
(41) Yang, A.; Li, D.; Lai, X.; Zhang, H.; Liang, C. Superhalogen Boron Tetrafluoride Surface Modification Reduces the Formation of Organic Cation Vacancies on the Surface of Halide Perovskite Films. *J. Phys. Chem. C* **2021**, *125*, 21223-21233.
(42) Zhang, H.; Xu, S.; Guo, T.; Du, D.; Tao, Y.; Zhang, L.; Liu, G.; Chen, X.; Ye, J.; Guo, Z.; et al. Dual Effect of Superhalogen Ionic Liquids Ensures Efficient Carrier Transport for Highly Efficient and Stable Perovskite Solar Cells. *ACS Appl. Mater. Interfaces* **2022**, *14*, 28826-28833.
(43) Zhu, S.; Wu, J.; Sun, W.; Pan, W.; Cai, F.; Liu, J.; Chen, L.; Chen, X.; Wang, C.; Wang, X. Interlayer Modification Using Phenylethylamine Tetrafluoroborate for Highly Effective Perovskite Solar Cells. *ACS Appl. Ener. Mater.* **2022**, *5*, 658-666.
(44) Liu, X.; Min, J.; Chen, Q.; Liu, T.; Qu, G.; Xie, P.; Xiao, H.; Liou, J. J.; Park, T.; Xu, Z. X. Synergy Effect of a pi-Conjugated Ionic Compound: Dual Interfacial Energy Level Regulation and Passivation to Promote V(oc) and Stability of Planar Perovskite Solar Cells. *Angew. Chem. Int. Ed.* **2022**, *61*, e202117303.
(45) Su, C.; Wang, R.; Tao, J.; Shen, J.; Wang, D.; Wang, L.; Fu, G.; Yang, S.; Yuan, M.; He, T. Fluoride-Assisted Crystallization Regulation Enables Efficient and Stable Wide-Bandgap Perovskite Photovoltaic. *J. Mater. Chem. A* **2023**, *11*, 6565-6573.
(46) Koh, J.; Kim, D.; Park, S. W.; Kim, H.; Hong, K.-H.; Shin, B. Selective Reactivity-Assisted Sacrificial Additive Coating for Surface Passivation of Wide Bandgap Perovskite Solar Cells with Cesium Tetrafluoroborate. *J. Mater. Chem. A* **2024**, *12*, 4290-4298.
(47) Wang, Z.; McMeekin, D. P.; Sakai, N.; van Reenen, S.; Wojciechowski, K.; Patel, J. B.; Johnston, M. B.; Snaith, H. J. Efficient and Air-Stable Mixed-Cation Lead Mixed-Halide

Perovskite Solar Cells with n-Doped Organic Electron Extraction Layers. *Adv. Mater.* **2017**, *29*, 1604186.
(48) Kogo, A.; Sanehira, Y.; Numata, Y.; Ikegami, M.; Miyasaka, T. Amorphous Metal Oxide Blocking Layers for Highly Efficient Low-Temperature Brookite TiO(2)-Based Perovskite Solar Cells. *ACS Appl. Mater. Interfaces* **2018**, *10*, 2224-2229.
(49) Pulvirenti, F.; Wegner, B.; Noel, N. K.; Mazzotta, G.; Hill, R.; Patel, J. B.; Herz, L. M.; Johnston, M. B.; Riede, M. K.; Snaith, H. J.; et al. Modification of the Fluorinated Tin Oxide/Electron-Transporting Material Interface by a Strong Reductant and Its Effect on Perovskite Solar Cell Efficiency. *Mol. Syst. Des. Eng.* **2018**, *3*, 741-747.
(50) Stolterfoht, M.; Wolff, C. M.; Márquez, J. A.; Zhang, S.; Hages, C. J.; Rothhardt, D.; Albrecht, S.; Burn, P. L.; Meredith, P.; Unold, T.; et al. Visualization and Suppression of Interfacial Recombination for High-Efficiency Large-Area pin Perovskite Solar Cells. *Nat. Energy* **2018**, *3*, 847-854.
(51) Schulz, P.; Cahen, D.; Kahn, A. Halide Perovskites: Is It All about the Interfaces? *Chem. Rev.* **2019**, *119*, 3349-3417.
(52) Ding, B.; Ding, Y.; Peng, J.; Romano-deGea, J.; Frederiksen, L. E. K.; Kanda, H.; Syzgantseva, O. A.; Syzgantseva, M. A.; Audinot, J. N.; Bour, J.; et al. Dopant-Additive Synergism Enhances Perovskite Solar Modules. *Nature* **2024**, *628*, 299-305.
(53) Akin, S.; Dong, B.; Pfeifer, L.; Liu, Y.; Graetzel, M.; Hagfeldt, A. Organic Ammonium Halide Modulators as Effective Strategy for Enhanced Perovskite Photovoltaic Performance. *Adv. Sci.* **2021**, *8*, 2004593.
(54) Kim, H.; Lee, S. U.; Lee, D. Y.; Paik, M. J.; Na, H.; Lee, J.; Seok, S. I. Optimal Interfacial Engineering with Different Length of Alkylammonium Halide for Efficient and Stable Perovskite Solar Cells. *Adv. Ener. Mater.* **2019**, *9*, 1902740.
(55) Amat, A.; Mosconi, E.; Ronca, E.; Quarti, C.; Umari, P.; Nazeeruddin, M. K.; Gratzel, M.; De Angelis, F. Cation-Induced Band-Gap Tuning in Organohalide Perovskites: Interplay of Spin-Orbit Coupling and Octahedra tilting. *Nano Lett.* **2014**, *14*, 3608-3616.
(56) Katoh, R.; Furube, A.; Yamanaka, K.-i.; Morikawa, T. Charge Separation and Trapping in N-Doped TiO2 Photocatalysts: A Time-Resolved Microwave Conductivity Study. *J. Phys. Chem. Lett.* **2010**, *1*, 3261-3265.
(57) Oga, H.; Saeki, A.; Ogomi, Y.; Hayase, S.; Seki, S. Improved Understanding of the Electronic and Energetic Landscapes of Perovskite Solar Cells: High Local Charge Carrier Mobility, Reduced Recombination, and Extremely Shallow Traps. *J. Am. Chem. Soc.* **2014**, *136*, 13818-13825.
(58) Nakajima, S.; Katoh, R. Time-Resolved Microwave Conductivity Study of Charge Carrier Dynamics in Commercially Available TiO2 Photocatalysts. *J. Mater. Chem. A* **2015**, *3*, 15466-15472.
(59) Hutter, E. M.; Hofman, J. J.; Petrus, M. L.; Moes, M.; Abellón, R. D.; Docampo, P.; Savenije, T. J. Charge Transfer from Methylammonium Lead Iodide Perovskite to Organic Transport Materials: Efficiencies, Transfer Rates, and Interfacial Recombination. *Adv. Ener. Mater.* **2017**, *7*, 1602349.
(60) Petrus, M. L.; Schutt, K.; Sirtl, M. T.; Hutter, E. M.; Closs, A. C.; Ball, J. M.; Bijleveld, J. C.; Petrozza, A.; Bein, T.; Dingemans, T. J.; et al. New Generation Hole Transporting Materials for Perovskite Solar Cells: Amide‐Based Small‐Molecules with Nonconjugated Backbones. *Adv. Ener. Mater.* **2018**, *8*, 1801605.

(61) Nishimura, N.; Kanda, H.; Katoh, R.; Kogo, A.; Murakami, T. N. Thermally Stable Phenylethylammonium-Based Perovskite Passivation: Spontaneous Passivation with Phenylethylammonium Bis(trifluoromethylsulfonyl)imide during Deposition of PTAA for Enhancing Photovoltaic Performance of Perovskite Solar Cells. *J. Mater. Chem. A* **2024**, *12*, 15631–15640.
(62) Nishimura, N.; Tachibana, H.; Katoh, R.; Kanda, H.; Murakami, T. N. Reactivity Manipulation of Ionic Liquid Based on Alkyl Primary Ammonium: Protonation Control Using Pyridine Additive for Effective Spontaneous Passivation of Perovskite via Hole Transport Material Deposition *ChemRxiv* **2024**. DOI: 10.26434/chemrxiv-2024-ts5k7
(63) García-Benito, I.; Quarti, C.; Queloz, V. I. E.; Orlandi, S.; Zimmermann, I.; Cavazzini, M.; Lesch, A.; Marras, S.; Beljonne, D.; Pozzi, G.; et al. Fashioning Fluorous Organic Spacers for Tunable and Stable Layered Hybrid Perovskites. *Chem. Mater.* **2018**, *30*, 8211-8220.
(64) Nishimura, N.; Tojo, M.; Takeoka, Y. Simple One-Step Synthesis of a Two-Dimensional Perovskite Consisting of Perfluoroalkyl-Based Ammonium Spacers Using Acetone as the Solvent. *Chem. Commun.* **2020**, *56*, 10293-10296.
(65) Yang, J.; Liu, C.; Cai, C.; Hu, X.; Huang, Z.; Duan, X.; Meng, X.; Yuan, Z.; Tan, L.; Chen, Y. High‐Performance Perovskite Solar Cells with Excellent Humidity and Thermo‐Stability via Fluorinated Perylenediimide. *Adv. Ener. Mater.* **2019**, *9*, 1900198.